Journal of Magnetism and Magnetic Materials 546 (2022) 168870

Contents lists available at ScienceDirect

Journal of Magnetism and Magnetic Materials

journal homepage: www.elsevier.com/locate/jmmm

Imaging of magnetic excitations in nanostructures with near-field microwave microscopy

Samuel Berweger [a], Robert Tyrell-Ead [a], Houchen Chang [b], Mingzhong Wu [b], Na Zhu [c], Hong X. Tang [c], Hans Nembach [a], T. Karl Stupic [a], Stephen Russek [a], T. Mitch Wallis [a], Pavel Kabos [a,*]

[a] Applied Physics Division, National Institute of Standards and Technology, Boulder, CO, USA
[b] Department of Physics, Colorado State University, Fort Collins, CO 80523, USA
[c] Department of Electrical Engineering, Yale University, New Haven, CT 06511, USA

ARTICLE INFO

Keywords:
Yttrium iron garnet (YIG)
Spin-waves
Microwave
Near-field microscopy

ABSTRACT

We present images of spin-wave excitations in a patterned yttrium iron garnet (YIG) thin film obtained by use of near-field microwave microscopy, which can achieve spatial resolution as high as 50 nm. Visualization of magnetic excitations is an enticing prospect for high-speed, high-density magnetic logic and storage applications, which has spurred the development of new magnetic microscopy and imaging techniques in recent years. Here we present a novel approach for local imaging of magnetic modes excited at room temperature with sub-diffraction-limited spatial resolution. This approach is based on a special atomic force microscope with broadband GHz capability for imaging the spatial distribution of dynamic magnetic excitations in patterned magnetic structures. Due to the inherent sub-wavelength, nanometer-scale spatial resolution of near-field scanning probe techniques, this approach has potential for a significant improvement in spatial resolution over optical techniques.

1. Introduction

The application of magnetic microscopies is critical for understanding dynamic magnetic excitations in patterned magnetic nanostructures. The ongoing push to increase the density of magnetic devices such as magnetic memory and logics has led to the development of novel approaches to measurement and imaging of nanoscale magnetic structures. Brillouin light scattering (BLS) – especially microfocus BLS [1,2,3] and time-resolved magneto-optic Kerr effect [4,5] techniques – have led to significant progress in understanding magnetic excitations. This experimental progress was critical for the study of the contribution of higher order magnon scattering processes to the damping in exchange biased films, [6,7,8] and the characterization and design of novel magnonic devices [9,10,11,12]. The constraining factor of the microfocus BLS method is that it is diffraction limited. Therefore, there is an ongoing effort to improve the spatial resolution and break the diffraction limit with novel techniques. These techniques include ferromagnetic resonance force microscopy, [13,14] scanning probe magneto-thermal microscopy, [15,16] time-resolved scanning transmission X-ray microscopy, [17] and near-field scanning microwave microscopy (NSMM) [18]. Other alternative methods to image propagating spin waves in magnonic devices are based on a scanning loop probes [19,20,21,22]. In addition to its capability to visualize magnetic excitations, microwave microscopy is an important experimental tool for validation of micromagnetic simulations as well as measurements of charge distributions in thin films and low-dimensional systems [18,23].

In this paper, our focus is on the application of NSMM to magnetic excitations. We present a local, spatially resolved technique with spatial resolution that is particularly suitable for micro- and nano-scale patterned structures and devices. The technique is based on a modified atomic force microscope (AFM) that can deliver a signal in the microwave frequency range (2 GHz to 26 GHz) to the AFM tip for local high-frequency electromagnetic measurements in addition to standard topographic imaging. The spatial resolution of this technique is on the order of 10 nm to 50 nm [24]. Below, we describe the technique and its application to measurements of spin-wave excitations in patterned 75 nm-thick yttrium iron garnet (YIG) films.

* Corresponding author.
E-mail address: pavel.kabos@nist.gov (P. Kabos).

https://doi.org/10.1016/j.jmmm.2021.168870
Received 25 June 2021; Received in revised form 10 November 2021; Accepted 22 November 2021
Available online 25 November 2021
0304-8853/Published by Elsevier B.V.

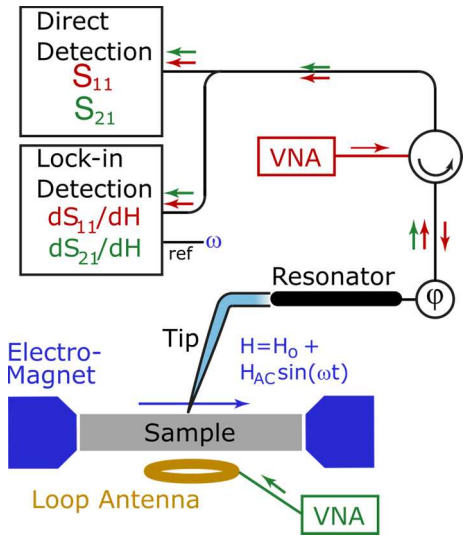

Fig. 1. Schematic of the near field scanning microwave microsocpe (NSMM) system used in the experiment. In reflection mode, the microwave signal path (red arrows) begins at a network analyzer source (red VNA), is reflected at the tip-sample junction, and is sent to the detectors via a circulator. In transmission mode, the signal path (green arrows) begins at a re-positioned network analyzer source (green VNA), is transmitted to the sample via a loop antenna, and transmitted through the sample and tip to the detectors. A small electromagnet generates an in-plane field H (blue arrow).

2. Sample preparation and properties

The patterned, low-loss, 75 nm-thick YIG film elements were fabricated using lithographically defined templates and radio frequency (RF) sputtering. The details of the YIG sample preparation are described in Ref. [25]. For the experiments presented in this work, the YIG sample consists of an array of 3 μm × 0.8 μm × 75 nm nano bars patterned over an area of 2 mm × 2 mm. The lattice spacing is 6 μm along the length direction and is 3 μm along the width direction. The aspect ratio of the nano bars is approximately 4:1, which gives rise to shape anisotropy along the length directions of the bars. The surface morphology of the patterned YIG samples was analyzed by conventional AFM. The crystalline structure was characterized through X-ray diffraction and X-ray reflection measurements. The magnetic hysteresis loop and ferromagnetic resonance measurements acquired at room temperature with an external magnetic field along the length direction of the YIG nano bars indicate a coercivity of about 2.4 kA/m (40 Oe), an effective anisotropy field of about 15.6 kA/m (195 Oe), and a ferromagnetic resonance linewidth of about 320 A/m (4 Oe) [26].

3. Experimental technique

A schematic drawing of a near-field scanning microwave microscope (NSMM) is shown in Fig. 1. This technique is sometimes referred to as scanning microwave impedance microscopy (sMIM) or simply scanning microwave microscopy (SMM). The system consists mainly of (1) an AFM with a specialized broadband cantilever (Rocky Mountain Nanotechnology®)*, (2) a cantilever holder mounted in a scanner head, (3) control electronics, (4) microwave electronics that bring microwave signals (2 GHz to 26 GHz) to the tip of the cantilever, and (5) an electromagnet that generates an in-plane magnetic field H. The cantilever is designed to transmit the microwave signal in the given frequency range and is connected to a half-wavelength resonator with a 50 Ω shunt resistor for signal enhancement. The microwave signal is typically delivered by a commercial vector network analyzer (VNA). A phase shifter (labeled ϕ in Fig. 1) is placed in series with the resonator. When the NSMM is operated at a single, fixed frequency, the phase shifter is used to match the impedance of the test platform to the impedance of the probe (resonator, tip, and sample) and thereby optimize the sensitivity of the NSMM. The system is equipped with a small electromagnet with a 2 mm gap between the two pole pieces, a winding for the sweep of the DC magnetic field, and an additional winding for the AC field modulation. The total field applied to the sample is the sum of the DC (H_o) and modulation ($H_{AC}\sin(\omega t)$) fields ($H_{AC} \ll H_o$). The maximum field that can be achieved in the magnet gap is 2 T (1600 kA/m). The system measures complex scattering parameters S_{ij} as well as the derivates dS_{ij}/dH, as illustrated in Fig. 1. Direct detection of S_{ij} can be carried out by use of an I/Q mixer as described in Ref. [23], or directly via the VNA. The derivatives dS_{ij}/dH are measured by use of a lock-in technique in which the H_{AC} modulation field frequency ω is used as the reference. The NSMM system can operate in two modes: (1) reflection mode, in which S_{11} is measured (signal reflected from the sample under test, as illustrated by red arrows in Fig. 1) or (2) transmission mode, in which S_{21} is measured (signal transmitted through the sample under test, as illustrated by green arrows in Fig. 1). For lock-in detection of dS_{11}/dH (reflection mode) or dS_{21}/dH (transmission mode), the modulation frequency ω is in the few hundred Hz range due to the frequency dependence of the inductance of the modulation coil.

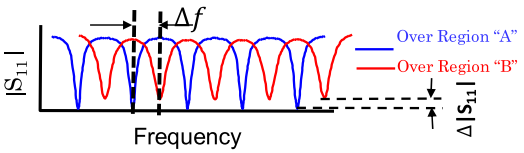

Fig. 2. Schematic representation of reflection S11 measurement with SMM.

S_{11} and S_{21} are functions of the impedance, Z, or the admittance, $Y = 1/Z$, of the probe-sample system. Local variations in Z or Y give rise to contrast in NSMM images. Z and Y depend on the local material properties at or near the tip position. These local properties include charge density, conductivity, permittivity, and permeability. Since both the reflection and transmission scattering parameters depend on Z, the frequency- and field- dependences of the magnetic susceptibility will be observable in the measured scattering parameters. For NSMM-based ferromagnetic resonance (FMR) measurements, a complete detailed description of the full contrast mechanism is quite involved and is beyond the scope of this paper. A description of the probe-sample interaction in an NSMM could be represented by an equivalent circuit model [27,28], including the dependence of equivalent circuit elements upon the complex magnetic susceptibility $\chi = \chi' - j\chi''$ [29].

A simplified sample geometry can be used to understand the fundamentals of probe response. Let's assume that the tip is moving over a sample with two different regions A and B that have distinct material properties and consequently present different impedances to the microscope tip. Due to the design of the cantilever, a series of resonances in the reflection coefficient S_{11} are detected in a broadband frequency sweep as shown in cartoon form in Fig. 2. Note that while the resonances in reflection mode appear as dips in the magnitude of S_{11}, resonances in transmission mode appear as peaks in S_{21}. Further, these resonances in the probe-based measurement are distinct from resonant magnetic excitations in the sample. For clarity, we refer to the latter as "modes" in the remainder of the paper. The broadband frequency sweep over region A in Fig. 2 is shown in blue. The sweep over region B is in red. Due to the change of the material properties, the set of resonant dips will shift in frequency. This shift of any specific resonant dip may be quantified by two parameters: the difference in the frequency Δf and the change in the magnitude ΔS_{11}. These changes represent the variations in the local tip-sample impedance that result from the changes in the local material properties. Their magnitudes, once measured, may be related to this tip-sample impedance Z (or admittance Y) and correspondingly to changes in the conductivity, the complex permittivity, and/or the complex permeability. In the present case, the contrast mechanism arises from

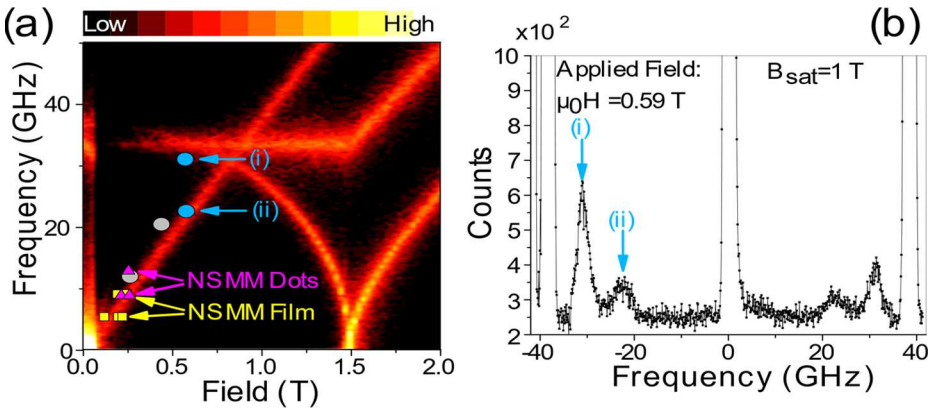

Fig. 3. Comparison of BLS and NSMM results obtained on nano-SAF dots. (a) The image shows the calculated field dependence of the dispersion relation for nano-SAF dots. Blue and gray circles represent the frequency of the mode peaks determined from measured BLS spectra. Magenta triangles and yellow squares represent the modes determined from measured NSMM spectra taken with the NSMM tip above nano-SAF dots (triangles) and a continuous SAF film (squares). (b) A representative BLS spectrum measured with an applied field of $\mu_0 H = 0.59$ T. Mode positions (i) and (ii) are labeled in both (a) and (b). The magnetic field was applied in the plane of the dots.

variations in the permeability of the magnetic material, which is itself a function of both H and operating frequency. In practice, one of the resonant dips in Fig. 2 is selected as an operating frequency. Once the operating frequency has been selected, the phase shifter is tuned to minimize the corresponding dip in the reflection coefficient (S_{11}). With the response of the NSMM tuned, sensitivity to changes in the local material properties is maximized: small changes in the local tip-sample impedance will lead to substantial Δf and ΔS_{11}.

Both imaging and spectroscopic measurements are employed here. To obtain an image of a magnetic excitation, the tip is raster scanned over the sample at a constant magnetic field and a constant operating frequency, and the signal (S_{11}, S_{21}, or the derivative of one of them) is measured at each tip position. Alternatively, to obtain a spectroscopic measurement, the magnetic field is swept at a fixed tip position and a fixed frequency, while the signal (S_{11}, S_{21}, or the derivative of one of them) is measured at each field value. For the initial approach of the cantilever and the control of the tip-sample distance during imaging, standard AFM feedback based on beam-bounce detection of the light by a quadrant photodetector is implemented. Further details of applications of this metrology can be found in review articles [18,27].

4. Validation

To validate the NSMM technique for characterization of magnetic excitations, we compare the BLS and NSMM measurements of nanoscale, synthetic antiferromagnets (SAFs). The SAFs are multi-layered structures consisting of two or more ferromagnetic layers that are separated by metallic spacers or insulating tunnel barriers and have antiparallel magnetizations [30]. In our case, they are represented by a stack of Ru 2 nm / CoFe 2 nm / Ru 0.8 nm / CoFe 4 nm / Ru 0.8 nm / CoFe 2 nm / Ru 2 nm, following the approach in [31]. The circular dot diameter was 1 μm and they formed a square array. The magnetic field was applied in the plane of the dots. The results of the comparison are shown in Fig. 3. The lines in Fig. 3a represent the calculated dispersion relation solving the Landau-Lifshitz equation applied to SAF dots [32]. The color bar indicates the low and high calculated signal amplitude. Blue and gray circles represent the spin-wave frequency for a given field as obtained from the mode peaks from measured BLS spectra. Magenta triangles and yellow squares correspond to the spin-wave modes determined from the NSMM spectra. NSMM spectra were acquired with the NSMM tip above the circular nano-SAF dots (triangles) and a continuous SAF film (squares). The spectra were acquired by measuring dS_{11}/dH at fixed NSMM operating frequencies as a function of the applied field. From the NSMM spectra the resonant field strength and mode amplitude can be extracted. Based on comparison of the BLS and NSMM measurements with the calculated dispersion for nano-SAF dots, we attribute the resonant modes observed in NSMM measurements to the excited spin-wave modes of the system. More broadly, this supports the extension of the technique to imaging of magnetic modes excited in patterned magnetic nanostructures.

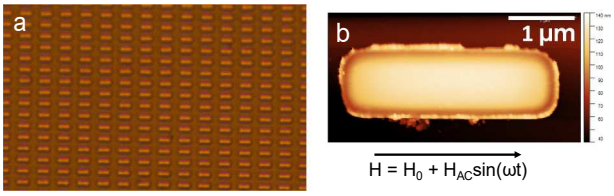

Fig. 4. a) Optical image of the patterned 2 mm × 2 mm YIG structure. b) AFM topography image of a single element of the array shown in (a).

5. Results

Having validated that the NSMM approach is sensitive to magnetic excitations, we applied it to thin-film, patterned YIG nanostructures to characterize the spatial distribution of magnetic excitations. Experimental results are obtained on a single element of the patterned array. An optical image of the array is shown in Fig. 4a and the AFM topography image of a single element from the array is shown in Fig. 4b.

The detailed topographic image of the single element shows the influence of the dry etching used to form the patterned structure. Note the roughness around the edges of the element. Fig. 4b also shows the orientation of the static (H_o) and modulation (H_{AC}) fields parallel to the long side of the patterned YIG element. Also note $H_{AC} \ll H_o$. As we discuss below, the field orientation shown in Fig. 4b has a strong influence on the observed spectrum and the excited spin-wave modes. The FMR linewidth of the patterned YIG nano bars is on the order of 320 A/m (4 Oe), which is low enough to obtain a clean local FMR response on a 75 nm-thick film.

Spatially resolved, spin excitation images were obtained in transmission mode (S_{21}) with the microwave signal transmitted to the tip (port 1) through the sample from by a 50 μm-diameter loop antenna (port 2) below the sample, as indicated in Fig. 1. The loop antenna has one end grounded and the other connected to the center conductor of a microstrip line. The system is designed in a way that the loop antenna is always under the cantilever tip in the scanner. An example of $|dS_{21}/dH|$ vs. field is shown in Fig. 5a. The displayed measurement was done at a fixed frequency of 6.62 GHz. The spikes in the image labeled with an arrow as "mode" correspond to the FMR response at the given field value. The non-resonant, off-mode response is labeled with an arrow as "background" in Fig. 5a. The inverted contrast at negative field values is due to the vectorial addition of the static and modulation fields, leading to a 180° phase change in the lock-in response between positive and negative static field values. As follows from the image in Fig. 4b there is a signal distribution over the sample even at the field corresponding to the background when the field is close to 0 mT. The image in Fig. 5c

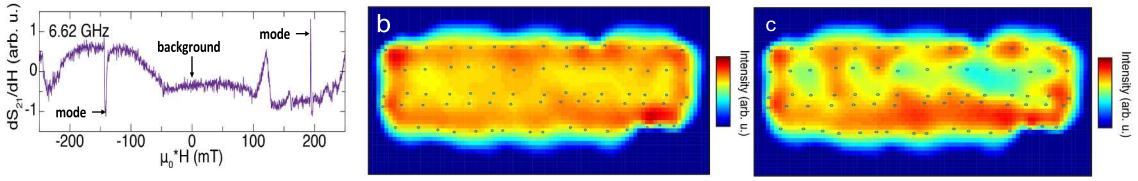

Fig. 5. a) Derivative signal in the middle of the sample as a function of the field; b) the image of the signal at each grid point at the background field value close to 0 mT; c) the image across the sample at the mode field value of ~ 200 mT. The images in b) and c) are 3 μm long.

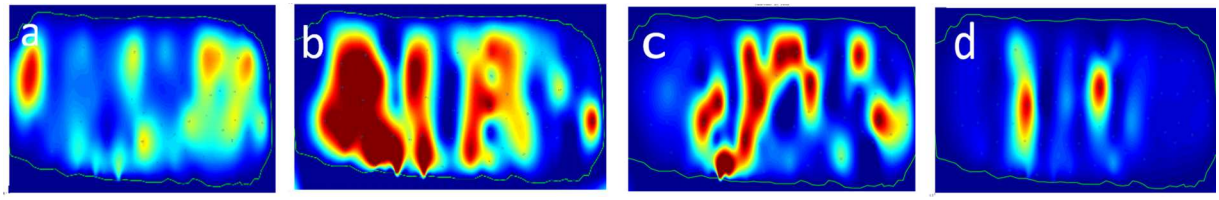

Fig. 6. dS21/dH signal magnitude distribution at 5.59 GHz for: a) 500 mT, b) 1300 mT, c) 1700 mT, and d) 2500 mT. The images were obtained from the measurement on the mentioned grid; in the post processing only the section around the patterned element is displayed, with the lateral dimension of 3 μm and the vertical dimension of 1 μm. The patterned YIG element boundary is illustrated as a thin green line. The dispalyed images are not to 4:1 scale and were adjusted to fit into the page width.

corresponds to the mode excitation at the field close to 200 mT. Therefore, to obtain the true mode distribution across the sample it is critical to acquire the images at both the mode and background field values. The spectral images like the one in Fig. 5a form the basis for extracting the image of mode distributions in patterned elements.

In order to visualize the magnetic excitations at different mode frequencies the topography image is divided into n × n pixels creating a n × n grid. At center of each pixel the spectral distribution as a function of the field at a given frequency are obtained. The obtained mode distribution images are processed from the acquired spectral distribution. For the presented mode distributions, a 16 × 16 pixel (1 pixel = 0.25 μm × 0.25 μm) grid that covers the sample and the surroundings represents the spatial resolution on the order of the optical methods. Naturally, the use of a finer grid with more points would improve the spatial resolution significantly below the optical resolution, albeit at the cost of increased detection time. To obtain the mode distribution across the patterned element, from each spectrum, the height of the mode at 200 mT is extracted and the background is subtracted, which is the value plotted at each pixel. Examples of processed NSMM images at an operating frequency of 5.59 GHz and at different field values are shown in Fig. 6a-d. The sequence of images in Fig. 6 corresponds to the measured $|dS_{21}/dH|$ pattern at 5.59 GHz for four different field values ranging from 550 mT to 2500 mT. The dS_{21}/dH amplitude distribution corresponds to the spatial profiles of magnetic modes at the respective fields. The red in the false color scheme corresponds to the high amplitude of the excitation. The shape of the patterned YIG element is represented by the thin green line.

6. Discussion

The results in Fig. 6 demonstrate the capability of the presented approach to visualize field- and frequency -dependent, magnetic excitations in patterned nanostructures. The images provide a detailed visualization of mode patterns within the single element as a function of the frequency and the field. The observation of a perturbed mode pattern is attributed to the local nonuniform field distribution of the patterned element that arises from shape nonuniformity and edge roughness. The observed patterns are not atypical; similar pattern distributions were predicted by finite element modeling as shown in [33].

The spatial resolution of the NSMM technique enables spatially resolved imaging of detailed mode patterns through the sample that clearly present the nonuniform excitation distribution usually predicted only by micromagnetic modeling at room temperature. The NSMM is a table-top system that operates under ambient conditions and is more straightforward to implement than other techniques, such as e.g., synchrotron X- ray dichroism spectroscopy. The discussed technique is based on a broadband atomic force microscope in the near field. Here, we demonstrated its applicability to local imaging of excitations in magnetic nanostructures. In [13] the local signal is detected as a force between the micromagnetic probe at the tip of the cantilever and the excitation, in the present case the signal detection is based on direct sensitivity to the change in the tip sample impedance due to the excited magnetization dynamics.

In conclusion, we demonstrated a scanning near-field microwave microscopy for sub-micrometer magnetic excitations in patterned structures and devices. Processed NSMM images that map the derivative of S_{21} with respect to H allow for local measurements of both the amplitude and phase of the magnetic excitations in nanometer scale structures. This information is not easily accessible with optical measurements, making the NSMM method an important complementary technique for characterization of micromagnetic structures. The technique does not require specialized sample preparation and is applicable to a variety of different materials and devices operating at and potentially above room temperature. The NSMM-based technique is compatible with conducting, semiconducting, and dielectric samples. The technique therefore provides an approach to high-resolution imaging of magnetic structures in a broad range of application areas, including spintronic, magnonic, sensing, neuromorphic, and biomagnetic applications, with spectroscopic precision and the potential for subsurface detection. Beyond the initial demonstration described here, future opportunities exist to fully model the NSMM probe-sample interactions for magnetic materials in the presence of magnetic fields. In turn, more detailed modeling will enable the development of calibrated, quantitative measurements of local susceptibility and permeability.

Declaration of Competing Interest

The authors declare that they have no known competing financial interests or personal relationships that could have appeared to influence the work reported in this paper.

Acknowledgement

The work at CSU was supported by the U.S. National Science

Foundation (EFMA-1641989; DMR-2002980). The work at Yale was supported by the NSF NewLaw grant (60061666).

*Contributions of the National Institute of Standards and Technology, not subject to copyright in the United States. Mention of commercial products is for informational purposes only, it does not imply NISTs recommendation or endorsement.

References

[1] S.O. Demokritov, V.E. Demidov, Micro-Brillouin Light Scattering Spectroscopy of Magnetic Nanostructures, IEEE Trans. Magn. 44 (1) (2008) 6–12.

[2] G. Gubbiotti, M. Madami, S. Tacchi, G. Carlotti, "Brillouin Light Scattering Study of Spin Dynamics in Patterned Nano -Elements: From Single-Layer to Multilayered Structures", in: Spin wave confinement edited by S. Demokritov, CRC Press, (2009, ebook 2019).

[3] J. Jersch, V.E. Demidov, H. Fuchs, K. Rott, P. Krzysteczko, J. Münchenberger, G. Reiss, S.O. Demokritov, Mapping of localized spin-wave excitations by near-field Brillouin light scattering, Appl. Phys. Lett. 97 (15) (2010) 152502, https://doi.org/10.1063/1.3502599.

[4] Y. Acremann, C.H. Back, M. Buess, O. Portmann, A. Vaterlaus, D. Pescia, H. Melchior, "Imaging Precessional Motion of the Magnetization Vector, Science 290 (5491) (2000) 492–495.

[5] B.C. Choi, M. Belov, W.K. Hiebert, G.E. Ballentine, M.R. Freeman, Ultrafast Magnetization Reversal Dynamics Investigated by Time Domain Imaging, Phys. Rev. Letters 86 (4) (2001) 728–731.

[6] S.M. Rezende, A. Azevedo, M.A. Lucena, F.M. de Aguiar, Anomalous spin-wave damping in exchange-biased films, Phys. Rev. B 63 (21) (2001), https://doi.org/10.1103/PhysRevB.63.214418.

[7] H.T. Nembach, J.M. Shaw, C.T. Boone, T.J. Silva, Mode- and Size-Dependent Landau-Lifshitz Damping in Magnetic Nanostructures: Evidence for Nonlocal Damping, Phys. Rev. Lett. 110 (11) (2013), https://doi.org/10.1103/PhysRevLett.110.117201.

[8] H.T. Nembach, R.D. McMichael, M.L. Schneider, J.M. Shaw, T.J. Silva, Comparison of measured and simulated spin-wave mode spectra of magnetic nanostructures, Appl. Phys. Lett. 118 (1) (2021) 012408, https://doi.org/10.1063/5.0039188.

[9] S.M. Rezende, Fundamentals of Magnonics, Springer, 2020.

[10] A.A. Serga, A.V. Chumak, B. Hillebrands, YIG Magnonics, J. Phys. D Appl. Phys. 43 (26) (2010) 264002, https://doi.org/10.1088/0022-3727/43/26/264002.

[11] P. Pirro, T. Brächer, A.V. Chumak, B. Lägel, C. Dubs, O. Surzhenko, P. Görnert, B. Leven, B. Hillebrands, Spin-wave excitation and propagation in microstructured waveguides of yttrium iron garnet/Pt bilayers, Appl. Phys. Lett. 104 (1) (2014) 012402, https://doi.org/10.1063/1.4861343.

[12] T. Sebastian, K. Schultheiss, B. Obry, B. Hillebrands, H. Schultheiss, Micro-focused Brillouin light scattering: imaging spin waves at the nanoscale, Front. Phys. 3 (2015), https://doi.org/10.3389/fphy.2015.00035 article 35.

[13] I. Lee, Y. Obukhov, G. Xiang, A. Hauser, F. Yang, P. Banerjee, D.V. Pelekhov, P. C. Hammel, Nanoscale scanning probe ferromagnetic resonance imaging using localized modes, Nature 466 (7308) (2010) 845–848.

[14] G. Wu, Y. Cheng, S. Guo, F. Yang, D.V. Pelekhov, P.C. Hammel, Nanoscale imaging of Gilbert damping using signal amplitude mapping, Appl. Phys. Lett. 118 (4) (2021) 042403, https://doi.org/10.1063/5.0023455.

[15] J.M. Bartell, D.H. Ngai, Z. Leng, G.D. Fuchs, Towards a table-top microscope for nanoscale magnetic imaging using picosecond thermal gradients, Nat. Commun. 6 (2015), https://doi.org/10.1038/ncomms9460.

[16] C. Zhang, J. M. Bartell, J. C. Karsch, I. Gray, and G. D. Fuchs, "Nanoscale magnetization and current imaging using scanning-probe magneto-thermal microscopy," Towards a table-top microscope for nanoscale magnetic imaging using picosecond thermal gradients," arXiv.org > cond-mat > arXiv:2102.02792 (2021).

[17] J. Förster, S. Wintz, J. Bailey, S. Finizio, E. Josten, C. Dubs, D.A. Bozhko, H. Stoll, G. Dieterle, N. Träger, J. Raabe, A.N. Slavin, M. Weigand, J. Gräfe, G. Schütz, Nanoscale X-ray imaging of spin dynamics in yttrium iron garnet, J. Appl. Phys. 126 (17) (2019) 173909, https://doi.org/10.1063/1.5121013.

[18] S. Berweger, T.M. Wallis, P. Kabos, Nanoelectronic Characterization: Using Near-Field Microwave Microscopy for Nanotechnological Research, IEEE Microwave Mag. 21 (10) (2020) 36–51, https://doi.org/10.1109/MMW.666810.1109/MMM.2020.3008305.

[19] K.R. Smith, M.J. Kabatek, P. Krivosik, M. Wu, Spin wave propagation in spatially nonuniform magnetic fields, J. Appl. Phys. 104 (4) (2008) 043911, https://doi.org/10.1063/1.2963688.

[20] Z. Wang, M. Cherkasskii, B.A. Kalinikos, L.D. Carr, M. Wu, Boris A Kalinikos, Lincoln D Carr, and Mingzhong Wu, "Formation of bright solitons from wave packets with repulsive nonlinearity", New J. Phys. 16 (5) (2014) 053048, https://doi.org/10.1088/1367-2630/16/5/053048.

[21] P.A.P. Janantha, P. Sprenger, M. Hoefer, M. Wu, Patrick Sprenger, Mark A Hoefer, and Mingzhong Wu, "Observation of self-cavitating envelope dispersive shock waves in yttrium iron garnet thin films", Phys. Rev. Lett. 119 (2) (2017) https://doi.org/10.1103/PhysRevLett.119.024101.

[22] E. Papa, S.E. Barnes, J.-P. Ansermet, Local Excitation of Magnetostatic Modes in YIG, IEEE Trans. Magn. 49 (3) (2013) 1055–1059.

[23] S. Berweger, G. Qiu, Y. Wang, B. Pollard, K.L. Genter, R. Tyrrell-Ead, T.M. Wallis, W. Wu, P.D. Ye, P. Kabos, Imaging Carrier Inhomogeneities in Ambipolar Tellurene Field Effect Transistors, Nano Lett. 19 (2) (2019) 1289–1294.

[24] K. Lee, M.I.B. Utama, S. Kahn, A. Samudrala, N. Leconte, B. Yang, S. Wang, K. Watanabe, T. Taniguchi, M.V.P. Altoé, G. Zhang, A. Weber-Bargioni, M. Crommie, P.D. Ashby, J. Jung, F. Wang, A. Zettl, Ultrahigh-resolution scanning microwave impedance microscopy of moiré lattices and superstructures, Sci. Adv. 6 (50) (2020), https://doi.org/10.1126/sciadv.abd1919.

[25] N. Zhu, H. Chang, A. Franson, T. Liu, X. Zhang, E. Johnston-Halperin, M. Wu, H. X. Tang, Patterned growth of crystalline Y3Fe5O12 nanostructures with engineered magnetic shape anisotropy, Appl. Phys. Lett. 110 (25) (2017) 252401, https://doi.org/10.1063/1.4986474.

[26] J. Ding, T. Liu, H. Chang, M. Wu, Sputtering Growth of Low-Damping Yttrium-Iron-Garnet Thin Films, IEEE Magn. Lett. 11 (2020) 1–5.

[27] S.M. Anlage, V.V. Talanov, A.R. Schwartz, Principles of Near-Field Microwave Microscopy, in: S. Kalinin, A. Gruverman (Eds.), Scanning Probe Microscopy, Springer New York, New York, NY, 2007, pp. 215–253, https://doi.org/10.1007/978-0-387-28668-6_8.

[28] T.M. Wallis, P. Kabos, Measurement Techniques for Radio Frequency Nanoelectronics, Cambridge University Press, Cambridge, 2017.

[29] T.J. Silva, H.T. Nembach, J.M. Shaw, B. Doyle, K. Oguz, K. O'brien, M. Doczy, Z. Ma, D.G. Seiler, Characterization of Magnetic Nanostructures for Spin-Torque Memory Applications with Macro- and Microscale Ferromagnetic ResonanceCharacterization of Magnetic Nanostructures for Spin-Torque Memory Applications with Macro- and Microscale Ferromagnetic Resonance, in: Chapter 16 in Metrology and Diagnostic Techniques for Nanoelectronics, Taylor and Francis Group, Jenny Stanford Publishing, 2016, https://doi.org/10.1201/9781315185385.

[30] R.A. Duine, K.-J. Lee, S.S.P. Parkin, M.D. Stiles, Synthetic antiferromagnetic spintronics, Nat. Phys. 14 (2018) 217–219.

[31] W. Hu, R.J. Wilson, C.M. Earhart, A.L. Koh, R. Sinclair, S.X. Wang, Synthetic antiferromagnetic nanoparticles with tunable susceptibilities, J. Appl. Phys. 105 (7) (2009) 07B508, https://doi.org/10.1063/1.3072028.

[32] S. Russek, E. Evarts and R.Usselman, Dynamics of Magnetic Nanoparticles and Nanodevices, Handbook of Nanomagnetism: Applications and Tools, Pan Stanford Publishing Pte. Ltd., Boca Raton, FL, [online], 2015. https://doi.org/10.1201/b18942-8.

[33] A.K. Mondal, C. Banerjee, A. Adhikari, A.K. Chaurasiya, S. Choudhury, J. Sinha, S. Barman, A. Barman, Spin-texture driven reconfigurable magnonics in chains of connected $Ni_{80}Fe_{20}$ submicron dots, Phys. Rev. B 101 (2020), 224426.